Cassini Imaging Science: Initial Results on Saturn's Rings and Small Satellites
C. C. Porco, *et al.*
Science **307**, 1226 (2005);
DOI: 10.1126/science.1108056

and reconnects with itself somewhere closer to the planet on the dawn side of the magnetotail.

This process results in a short, closed magnetic field line that is nearly empty of plasma, and a closed magnetic loop that contains a large amount of heavy ions. The heavy, closed loop (the plasmoid) moves down the magnetotail and eventually leaves Saturn's magnetosphere. According to a preliminary analysis of the simulation results, the loading-unloading process is quasi-periodic, with plasmoids launching at multiples of Saturn's rotation period (the largest ejection occurs approximately every four rotations). This time period is probably controlled by the mass-loading rate and is modulated by the planetary rotation.

Cassini is the first planetary mission that can "image" a magnetosphere by detecting energetic neutral atoms created by charge transfer. It does so with the MIMI instrument, which has already made an exciting discovery: the existence of a radiation belt inside Saturn's innermost ring. This radiation belt is probably formed by the interaction between the main radiation belt and the upper layers of Saturn's exosphere. The nightside source of energetic neutral particles varies with an ~11-hour periodicity, whereas the source on the dayside remains approximately constant (6).

The vast improvement of Cassini's instruments over those on Voyager has resulted in a wealth of information about the plasma composition in the magnetosphere. Data from the high-resolution mass spectrometers CAPS and MIMI show that the inner magnetosphere is mainly dominated by hydrogen (H^+, H_2^+) and water-group ions (OH^+, H_2O^+, H_3O^+, O^+, O_2^+) (5–7).

Voyager's instruments could not differentiate water-group ions from nitrogen ions. With such differentiation now possible, the very low abundance of N^+ and N_2^+ in the magnetosphere is striking. Nitrogen ions escaping from Titan were expected to be the dominant species near Titan's orbit, but this is not the case. It remains unclear whether the low nitrogen abundance is due to reduced atmospheric escape from Titan or to a process that rapidly removes these ions from the magnetosphere.

Saturn's rings are one of the solar system's most spectacular phenomena. Cassini instruments have discovered a new element to this system: a tenuous atmosphere and ionosphere above the rings (2, 4–7). The main constituent of the ring particles is assumed to be water ice, which produces a cloud of water products due to photo-processes and sputtering. Waite et al. suggest (7) that O_2 is the main constituent of the ring atmosphere; it can be produced by radiation-induced decomposition of ice. MIMI discovered a depletion of energetic ions and electrons inside Dione's orbit that is probably related to the higher-than-expected neutral gas density in this region. The most intriguing constituent of the ring-plane ionosphere is H_3O^+ (5). This ion is the major constituent of the dense ionospheres of comets and is produced via $H_2O^+ + H_2O \rightarrow H_3O^+ + OH$. The composition changes dramatically beyond ~9 Saturn radii to H^+-dominated plasma.

The new observations of Saturn's magnetosphere (2–7) paint a consistent picture of a highly dynamic magnetosphere dominated by inner plasma sources and planetary rotation but with substantial solar wind control. Cassini's first pass through the Saturn system has revealed a magnetosphere that, although familiar, holds many mysteries. The fun has begun.

References and Notes
1. M. Blanc et al., Space Sci. Rev. **104**, 253 (2002).
2. L. W. Esposito et al., Science **307**, 1251 (2005).
3. M. K. Dougherty et al., Science **307**, 1266 (2005).
4. D. A. Gurnett et al., Science **307**, 1255 (2005).
5. D. T. Young et al., Science **307**, 1262 (2005).
6. S. M. Krimigis et al., Science **307**, 1270 (2005).
7. J. H. Waite et al., Science **307**, 1260 (2005).
8. S. Jurac, J. D. Richardson, J. Geophys. Res., in press.
9. A. Sánchez-Lavega, Science **307**, 1223 (2005).
10. The simulations were carried out with the University of Michigan's three-dimensional magnetohydrodynamic code, BATS-R-US (11).
11. K. G. Powell et al., J. Comput. Phys. **154**, 284 (1999).
12. This work was supported by the NASA Cassini Project under contract JPL-961178. The authors acknowledge the help of D. De Zeeuw in preparing the figure.

RESEARCH ARTICLE

Cassini Imaging Science: Initial Results on Saturn's Rings and Small Satellites

C. C. Porco,[1]* E. Baker,[1] J. Barbara,[2] K. Beurle,[3] A. Brahic,[4] J. A. Burns,[5] S. Charnoz,[4] N. Cooper,[3] D. D. Dawson,[6] A. D. Del Genio,[2] T. Denk,[7] L. Dones,[8] U. Dyudina,[9] M. W. Evans,[3] B. Giese,[10] K. Grazier,[11] P. Helfenstein,[5] A. P. Ingersoll,[9] R. A. Jacobson,[11] T. V. Johnson,[11] A. McEwen,[6] C. D. Murray,[3] G. Neukum,[7] W. M. Owen,[11] J. Perry,[6] T. Roatsch,[10] J. Spitale,[1] S. Squyres,[5] P. Thomas,[5] M. Tiscareno,[5] E. Turtle,[6] A. R. Vasavada,[11] J. Veverka,[5] R. Wagner,[10] R. West[11]

Images acquired of Saturn's rings and small moons by the Cassini Imaging Science Subsystem (ISS) during the first 9 months of Cassini operations at Saturn have produced many new findings. These include new saturnian moons; refined orbits of new and previously known moons; narrow diffuse rings in the F-ring region and embedded in gaps within the main rings; exceptionally fine-scale ring structure in moderate– to high–optical depth regions; new estimates for the masses of ring-region moons, as well as ring particle properties in the Cassini division, derived from the analysis of linear density waves; ring particle albedos in select ring regions; and never-before-seen phenomena within the rings.

Major objectives of the Cassini Imaging Science investigation were the search for new satellites of Saturn within and external to the rings and determination of their orbits; refinement of the orbits of the known satellites; investigation of the temporal evolution of all satellite orbits; search for ring spokes; characterization of ring color and particle photometric properties; and the investigation of ring structure, dynamics, and temporal evolution, including interactions between rings and moons (1).

From 9 February 2004 to 1 June 2004, Cassini's narrow angle camera (NAC) (1) took ~800 images in four separate sequences designed specifically to search for new moons among the major icy saturnian satellites. A fifth sequence of 94 wide-angle frames designed to simultaneously image faint rings and search for new moons among the known moons was taken in October 2004 after Cassini entered orbit (2) (table S1).

Two new satellites orbiting between Mimas and Enceladus, S/2004 S1 (provisionally named Methone) and S/2004 S2 (provisionally named Pallene), were first seen in 1.2- and 4.6-s exposures taken on 1 June 2004 (3). [Contrary to earlier speculation (3),

Fig. 1. Contrast-enhanced images showing newly discovered F-ring objects S/2004 S3 (**A**), S/2004 S4 (**B**), and S/2004 S6 (**C**). S/2004 S3 is shown in image N1466489981 taken on 21 June 2004 with a radial scale of 55 km/pixel and a phase angle of 66°. S/2004 S4 is shown in image N1466513582 taken on 21 June 2004 with a radial scale of 59 km/pixel and a phase angle of 66°. S/2004 S6 is shown in image N1477693877 taken on 28 October 2004 with a radial scale of 4.3 km/pixel and a phase angle of 151°.
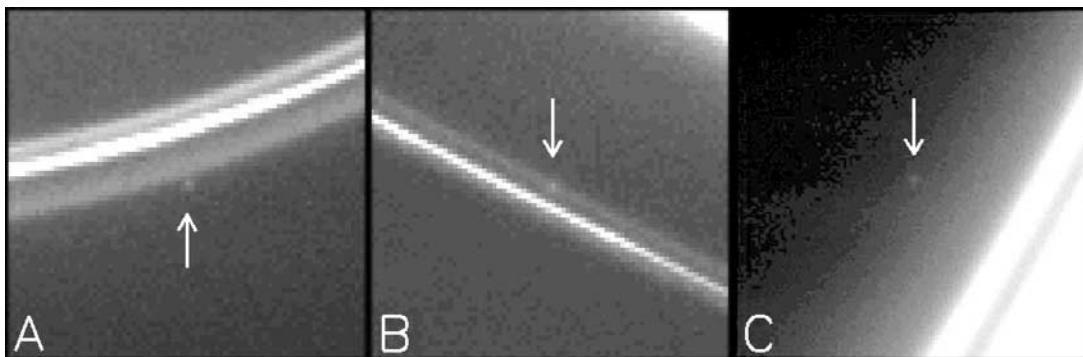
it has been determined that the new moon Pallene is the same body as S/1981 S14, which was seen in one Voyager 2 image.] A third main-satellite region moon, S/2004 S5 (provisionally named Polydeuces), was found in a series of 5.6-s exposures in the fifth sequence (*4*). It is a trailing co-orbital of Dione.

Satellite searches were also conducted within the main ring system, including the F ring region. Three new objects were sighted. Two objects (S/2004 S3 and S/2004 S6) were detected in ring ansa movie sequences taken during June and October; another, S/2004 S4, was found in a ring photometry sequence, also on 21 June 2004, taken 5 hours after the first sighting of S/2004 S3 (*4*, *5*) (Fig. 1). The object S/2004 S3 clearly orbits outside the core of the F ring and outside the outer F-ring strand; S/2004 S4 and S/2004 S6 orbit interior to the F ring, the former within the inner F-ring strand and the latter interior to it. It is not clear at present whether these objects are moons or clumps (*6*).

No disk-resolved images of any of the new satellites have yet been taken. Size estimates have been made by assuming appropriate disk-integrated reflectivities (*7*) and taking into account the solar phase angle and the pixel size in kilometers to compute observed I/F values and subsequently derive a surface area (*2*). This calculation yielded approximate diameters of 3, 4, and 3.5 km for Methone, Pallene, and Polydeuces, respectively; S/2004 S3, S/2004 S4, and S/2004 S6 were found to be ~5 km across, assuming they are moons. Based on this method, Atlas, which orbits closely outside the A ring, and Pan, which orbits within the 325-km-wide Encke gap in the outer A ring, were found to be 20 and 25.6 km across, respectively, contrary to Voyager results (32 and 20 km, respectively) that suggested that Atlas was the larger of the two.

The objects S/2004 S3, S/2004 S4, and S/2004 S6 occupy a region near the F ring that is expected to produce chaotic orbits (*8*, *9*). No orbital integrations of satellites and ring particles in this region, aimed at examining the stability of these new bodies, have yet been performed.

The dynamical stability, and even the existence, of small objects like Methone, Pallene, and Polydeuces orbiting among the major saturnian satellites provide insight into their dynamical evolution and the history of impactors within the saturnian system. The result of a 4800-year integration of orbital motions of test particles in the vicinity of Mimas (*2*), (fig. S1), five times longer than previous integrations (*10*), shows that the region close to Mimas is very perturbed, and particles within ~0.2R_s of Mimas are excited into eccentric and inclined orbits. (1R_s is one Saturn radius, equal to 60,330 km.) Methone, very close to Mimas's region of influence, might be expected to have a substantial eccentricity and inclination, yet it does not (Table 1). Pallene is in a quiescent region and might be expected to have a smaller eccentricity and inclination, yet it does not.

A longer data arc than currently available will likely be necessary to reveal the effects of Mimas's perturbation on Methone. However, several explanations are possible for the eccentric and inclined orbit of Pallene: (i) a secular gravitational effect that is not manifest in only ~4800 years' integration; (ii) the moon migrated across eccentricity- and inclination- exciting resonances to its present position; or (iii) it is a fragment of a parent body that was hit by an impactor on an eccentric orbit. The third scenario could indicate possible heavy cometary bombardment in the past (*2*).

Many Cassini images were planned to refine the orbits of the known small moons; many other images targeted to Saturn or the rings capture these bodies serendipitously. Once their orbits were determined, new moons discovered in satellite searches were recovered in subsequent retargeted observations (*4*). Positional measurements of stars and moons made in these Cassini images plus an accurate description of the spacecraft trajectory form the basic data used to perform image navigation and determine the orbits of all satellites over the time interval spanned by the data.

The classical elements for the eight very small (<25-km diameter) satellites observed by Cassini ISS appear together with their standard errors in Table 1. The model for most of the satellite orbits is a Keplerian ellipse referred to the latest Cassini-era Saturn equator with apse and node rates determined by Cassini-era values for Saturn's gravitational harmonics (*2*). [Where Voyager data were available for Pan and Atlas, these have been used in the orbital fits (*2*).] However, because Polydeuces was found librating around Dione's trailing L5 Lagrangian point, its orbit was determined by performing a numerical integration to all the observations, including the perturbations due to the major saturnian satellites and the oblateness of Saturn. Polydeuces is librating ~68° behind Dione, with an amplitude of 25.8° and a period of 792 days. Dione's previously known Lagrangian satellite, Helene, leads Dione by ~62° and librates with an amplitude of 14.8° and a period of 769 days (*11*). These amplitudes are considerably larger than the 1.3° and 3.6° libration amplitudes of the leading and trailing co-orbitals of Tethys, Telesto, and Calypso. A set of mean orbital elements was developed for Polydeuces by fitting a precessing ellipse to the integration over the time span 1 January 2004 to 1 January 2009, but correcting the mean longitude to account for the libration.

[1]Cassini Imaging Central Laboratory for Operations, Space Science Institute, 4750 Walnut Street, Suite 205, Boulder, CO 80301, USA. [2]Goddard Institute for Space Studies, NASA, 2880 Broadway, New York, NY 10025, USA. [3]Astronomy Unit, Queen Mary, London E1 4NS, UK. [4]Centre d'Etudes de Saclay, Université Paris 7, L'Orme des Merisiers, 91191 Gif sur Yvette Cedex, France. [5]Department of Astronomy, Cornell University, Space Sciences Building, Ithaca, NY 14853, USA. [6]Department of Planetary Sciences, University of Arizona, 1629 East University Boulevard, Tucson, AZ 85721, USA. [7]Institut für Geologische Wissenschaften, Freie Universität, 12249 Berlin, Germany. [8]Department of Space Studies, Southwest Research Institute, 1050 Walnut Street, Suite 400, Boulder, CO 80302, USA. [9]Division of Geological and Planetary Sciences, California Institute of Technology, 150-21, Pasadena, CA 91125, USA. [10]Institute of Planetary Research, German Aerospace Center, Rutherfordstrasse 2, 12489 Berlin, Germany. [11]Jet Propulsion Laboratory, California Institute of Technology, 4800 Oak Grove Drive, Pasadena, CA 91109, USA.

*To whom correspondence should be addressed. E-mail: carolyn@ciclops.org

Table 1. Planetocentric elements of the small saturnian moons. The epochs are given as Julian ephemeris dates. A sufficient number of observations of all satellites, with the exception of S/2004 S4, were available to permit the determination of a full set of elements for each. For S/2004 S4, we fit a circular equatorial orbit to the observations. Polydeuces is a trailing co-orbital of Dione with a large amplitude of libration. The set of mean orbital elements given here for Polydeuces was developed by fitting a precessing ellipse to the integration over the time span 1 January 2004 to 1 January 2009 and correcting the mean longitude to account for the libration. We compute the values of a, $d\varpi/dt$, or $d\Omega/dt$ from the formulae given in (75); their uncertainties stem from the errors in the satellites' mean motions and the error in the second zonal harmonic of Saturn's gravity field.

Element	Atlas (SXV)	Pan (SXVIII)	Methone (S/2004 S1)
Epoch	2,453,177.5	2,453,177.5	2,453,177.5
a (km)	137,665.0 ± 1.0	133,584.0 ± 1.0	194,251.0 ± 1.0
e ($\times 10^3$)	1.20 ± 0.06	0.21 ± 0.08	1.0 ± 0.2
i (°)	0.009 ± 0.007	0.007 ± 0.002	0.018 ± 0.007
λ (°)	11.398 ± 0.008	146.611 ± 0.008	194.76 ± 0.02
ϖ (°)	82.3 ± 3.6	249.0 ± 10.0	348.0 ± 18.0
Ω (°)	281.0 ± 27.0	303.0 ± 40.0	351.0 ± 29.0
$d\lambda/dt$ (°/day)	598.313997 ± 0.000003	626.031719 ± 0.000004	356.5365 ± 0.0002
P_λ (s)	51,986.0811 ± 0.0003	49,684.3834 ± 0.0003	87,239.31 ± 0.4
$d\varpi/dt$ (°/day)	2.8812 ± 0.0012	3.2068 ± 0.0014	0.8540 ± 0.0003
$d\Omega/dt$ (°/day)	−2.8674 ± 0.0012	−3.1905 ± 0.0014	−0.8519 ± 0.0003

Element	Pallene (S/2004 S2)	S/2004 S3	S/2004 S4
Epoch	2,453,177.5	2,453,177.5	2,453,177.5
a (km)	212,283.0 ± 1.0	141,071.0 ± 1.0	140,171.0 ± 41.0
e ($\times 10^3$)	4.0 ± 0.2	4.0 ± 0.2	0.0
i (°)	0.181 ± 0.008	0.05 ± 0.02	0.0
λ (°)	125.48 ± 0.05	29.90 ± 0.02	27.9 ± 0.1
ϖ (°)	78. ± 7.0	154. ± 4.0	
Ω (°)	7.0 ± 6.0	188.0 ± 14.0	
$d\lambda/dt$ (°/day)	312.0271 ± 0.0009	576.7104 ± 0.0006	582.3 ± 0.3
P_λ (s)	99,683.6 ± 0.3	53,933.48 ± 0.05	53,417.0 ± 24.0
$d\varpi/dt$ (°/day)	0.6243 ± 0.0002	2.6414 ± 0.0008	
$d\Omega/dt$ (°/day)	−0.6230 ± 0.0002	−2.6295 ± 0.0008	

Element	Polydeuces (S/2004 S5)	S/2004 S6
Epoch	2,453,006.5	2,453,177.0
a (km)	377,390.0	140,760.0 ± 12.0
e ($\times 10^3$)	18.2	7.5 ± 1.5
i (°)	0.1705	0.02 ± 0.01
λ (°)	107.58	27.0 ± 10.0
ϖ (°)	143.19	240.0 ± 20.0
Ω (°)	302	25.0 ± 5.0
$d\lambda/dt$ (°/day)	131.53	578.63 ± 0.08
P_λ (s)	236,468	53,755.0 ± 7.0
$d\varpi/dt$ (°/day)	0.0889	2.6626 ± 0.0009
$d\Omega/dt$ (°/day)	−0.0773	−2.6504 ± 0.0009

Table 2. Planetocentric mean elements of Janus, Epimetheus, Prometheus, and Pandora at Julian ephemeris date 2453005.50 referred to the Saturn equator. These are the elements of a precessing ellipse fit to the integration from 1 January 2004 to 1 January 2005. This interval avoids the time of closest approach for Janus and Epimetheus (February 2006) and the time of anti-apse alignment for Prometheus and Pandora (late 2006). Thus, the quoted orbital elements are free of the effects of the gravitational interactions between the satellites. The mean orbits during this interval, however, exhibit periodic differences from the integrated ones, with the largest differences being in the along-orbit direction. The amplitudes of the differences are about 200, 900, 200, and 1000 km for Janus, Epimetheus, Prometheus, and Pandora, respectively. The integrated orbits themselves are presumed to be accurate to better than 150 km for Janus, Epimetheus, and Pandora and 300 km for Prometheus.

Element	Janus	Epimetheus	Prometheus	Pandora
a (km)	151,460.0	151,410.0	139,380.0	141,710.0
e	0.0067	0.0098	0.0023	0.0042
i (°)	0.1649	0.3541	0.0056	0.0522
λ (°)	171.4792	346.0186	306.1799	252.6616
ϖ (°)	288.2511	38.5429	63.2935	50.4554
Ω (°)	48.1413	85.5628	266.0754	329.9818
$d\lambda/dt$ (°/day)	518.238639	518.483719	587.284953	572.792057
P_λ (days)	0.6947	0.6943	0.6130	0.6285
$d\varpi/dt$ (°/day)	2.0528	2.0552	2.7573	2.5994
$d\Omega/dt$ (°/day)	−2.0447	−2.0472	−2.7445	−2.5877

The addition of the Cassini data has improved knowledge of the mean longitude rates of Atlas and Pan by four and three orders of magnitude, respectively, over their previously published values. No significant inclination has been detected in the orbit of Atlas. However, the orbits of both, especially that of Atlas, exhibit a measurable eccentricity and Pan looks to have a significant, though very small, inclination. There are no important resonances within a resonance width of Pan's orbit that might affect its orbit, and no other comparably sized moons have been found in the Encke gap. Hence, we conclude that Pan's eccentricity is derived from its interactions with the surrounding ring material, a result that is sure to shed light on the mechanism by which exosolar planets embedded in disks derive their eccentricities (12).

Table 2 contains a set of mean elements for the "co-orbital" moons, Janus and Epimetheus, and the F-ring shepherds, Prometheus and Pandora, derived from both Cassini and earlier measurements (2). Because of strong dynamical interactions between the members of each pair, the orbits of these moons were numerically integrated (13).

Saturn's rings were imaged regularly on approach to Saturn and then immediately following Saturn orbit insertion (SOI) when the spacecraft came within 16,000 km above the unilluminated side of the rings. The SOI darkside sequence resulted in image scales in the ring plane between ~100 and 350 m/pixel. This series of narrow-angle SOI-darkside images (which, because of spacecraft motion, does not form a complete, uninterrupted scan of the rings) begins in the outer C ring, crosses into the inner B ring, skips the middle B ring, and captures the outer B ring, Cassini division, and the breadth of the A ring. Immediately following this period, the spacecraft crossed the ring plane and acquired a series of dayside NAC and (simultaneous) WAC (wide angle camera) images, extending from the F ring inward and terminating just interior to the Encke gap. These SOI-dayside NAC images have radial scales of ~1 km/pixel, several times coarser than the dark-side images but with five times better resolution than anything acquired by Voyager. The total number of images acquired during the dark- and lit-side post-SOI period was 85.

Nine days before it entered orbit around Saturn, Cassini imaged the lit face of the main rings with the NAC in five broadband filters (1): UV3 (338 nm), BL1 (451 nm), GRN (568 nm), RED (650 nm), and IR2 (862 nm), at a phase angle of 66° and an image scale of 38 km/pixel (Fig. 2). We constructed ring spectra (Fig. 3), using overall, or Bond, albedos of the ring particles as a function of distance from Saturn and wavelength that we inferred by using a classical multiple-scattering code (2) (fig. S2).

Spectra of the rings in 12 regions similar to those considered by (14) show that the

largest variations in spectral slope occur at short wavelengths (15). The B ring is generally "redder" than the A ring, which, in turn, is redder than the C ring and Cassini division (Fig. 3) (16). Because the rings' scattering function is insensitive to the physical thickness of the rings in this intermediate-phase viewing geometry, our spectra provide evidence that most small-scale variations in ring brightness result from compositional differences (17, 18). If the rings began as nearly pure water ice, regions of smaller optical depth are expected to become more polluted by interplanetary dust, resulting in reduced particle albedos (19, 20).

Spokes, the transient, quasi-radial ghostly features observed by Voyager in Saturn's B ring (21) and seen also in Hubble Space Telescope (HST) images (22), were not seen in any Cassini image taken on approach to Saturn, during which the solar incidence angle was ~65° and the emission angle was ~73°. Radiative transfer modeling of HST observations of spokes indicated that they might be seen when either the spacecraft or Sun's elevation angle above the ring plane got below ~7° (22). Such a grazing viewing geometry occurred for Cassini on its first periapse passage by Saturn after SOI during October 2004. However, no spokes were observed at that time either. The creation and/or visibility of spokes may depend critically on the Sun's elevation above the rings. High Sun creates a layer of photoelectrons above the rings that can negatively charge small dust particles above the rings, pulling them back to the (positively) charged rings. A low solar elevation angle reduces the number density in the photoelectron layer, causing dust particles to have a net zero (or slightly positive) charge and therefore to be repelled by the positively charged ring (23). The relatively high Sun elevation at present may create an environment hostile to the appearance of spokes. If this is true, spokes may not become visible until later in the orbital tour when the Sun's elevation is lower.

The highest resolution images taken shortly after SOI have revealed new ring phenomena as well as new details at higher signal-to-noise (S/N) ratios than previously achieved on ring features—e.g., gap edges, narrow ringlets, spiral density and bending waves—first seen in Voyager occultation scans or images. Moreover, with two-dimensional images, one can confidently distinguish real, longitudinally extended ring features from noise, a problem that hampers the interpretation of low–S/N Voyager occultation data taken in high–optical depth regions of Saturn's rings. Many of our findings now provide new insights into the ring particles' collective effects (e.g., collisions, viscosity, self-gravity) and how these effects are altered in the presence of gravitational perturbations by moons.

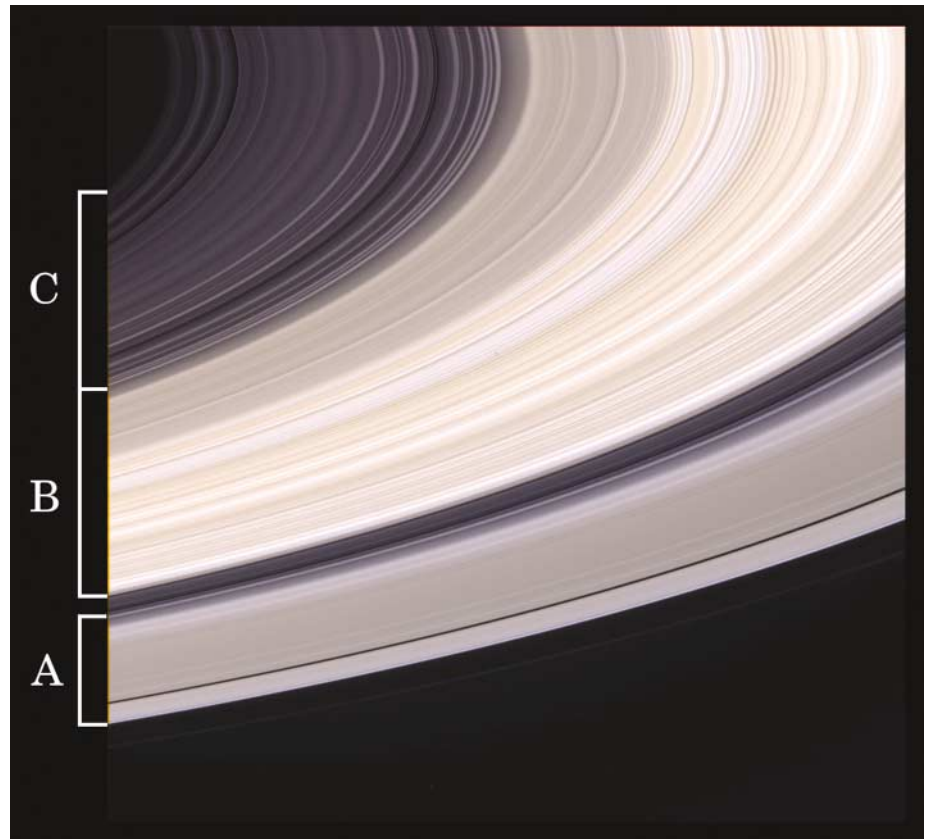Two ring regions of interest, captured in the dark-side SOI images (24), are shown in

Fig. 2. Nine days before it entered orbit, Cassini captured this natural color view of Saturn's rings using the BL1 (451 nm), GRN (568 nm), and RED (650 nm) filters. The images that comprise this composition were obtained with the narrow-angle camera on 21 June 2004, from a distance of 6.4 million km from Saturn and a phase angle of 66°. The image scale is 38 km/pixel. Many bands throughout the B ring have a pronounced sandy color; other subtle variations in color are obvious. Color variations in Saturn's rings have previously been seen in Voyager and Hubble Space Telescope (HST) images. Cassini images show that color variations across the rings are more pronounced in this viewing geometry (i.e., at intermediate phase angle) than they were when seen from HST at phase angles no greater than 6°. The different colors in the rings reflect different amounts of contamination of the predominant constituent—water ice—by other materials such as silicates or organics.
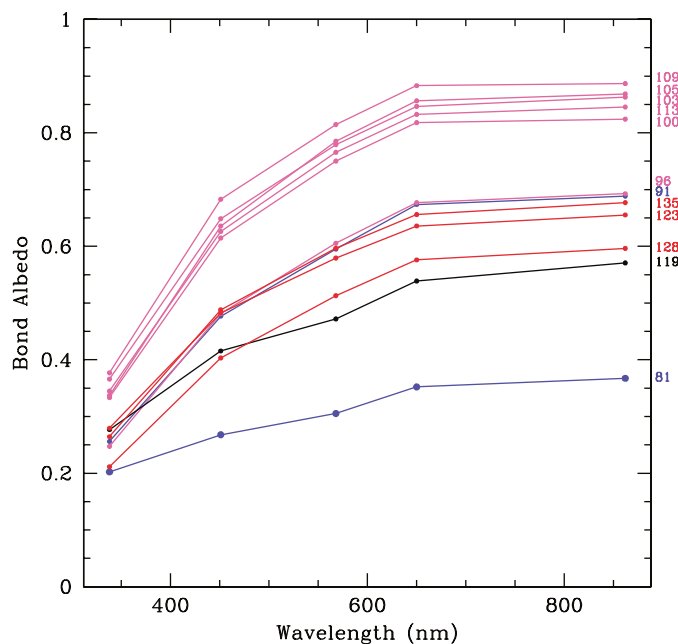

Fig. 3. Spectra of selected regions in Saturn's main rings. The main ring divisions are color-coded. This plot includes two regions in the C ring (blue), six regions in the B ring (green), one region in the Cassini division (black), and three regions in the A ring (red). Curves are labeled with the region's mean distance from Saturn's center in units of 1000 km.

Fig. 4. Figure 4A captures the narrow, eccentric Maxwell ringlet (25) in the gap of the same name at a resolution comparable to that of the Voyager stellar and radio occultation scans but at a higher S/N ratio. The Maxwell ring is analogous to the ε ring of Uranus in many of its physical and kinematic properties (26). A wave in the middle of the Maxwell ring, not discernible in the noisy Voyager occultation scans, is visible in the image and in a longitudinally averaged radial scan across the image (fig. S3a). A wave, presumably generated by the Cordelia 47:49 outer eccentric resonance (OER) (27), is observed in the middle of the uranian ε ring (28), but the wave in the Maxwell ring is not associated with any known resonance. No moon has yet been discovered in this gap either. The Maxwell ring wave is remarkably similar to waves produced by pulsation instabilities (also known as viscous overstabilities) in simulations of narrowly confined viscous rings (29), in which the narrow ring acts like a resonant cavity for amplifying a free wave disturbance. In this case, the pulsation frequency is comparable to the precession frequency and nonlocal transport of angular momentum dominates the viscous stresses. This suggestion can be verified by examining the correlation of vertical thickness of the ring with optical thickness in the wave in upcoming Cassini stellar and radio occultation data.

Figure 4B shows the narrow, eccentric Huygens ringlet on the left in the gap of the same name, a very narrow ringlet to the right of it, and one of the broad, low–optical depth (τ ∼ 0.1) plateaus for which the Cassini division is renowned. Figure S3b shows a longitudinally averaged radial scan of the Huygens ringlet seen in this image. This ringlet is known to have a very nonlinear width-radius relation (30). Here the ringlet is seen near its most narrow profile, and yet it appears near its most extreme radial extent. Cassini images reveal it to have a radial profile quite distinct from the Maxwell ringlet (fig. S3a), with optically thick ring edges. These observations may be related to the fact that the Huygens ringlet is the one narrow saturnian ring discovered so far to support two normal modes, one of which may be excited by a combination of the nearby Mimas 2:1 inner Lindblad resonance (ILR) and the eccentric outer B-ring edge (30, 31). The optically thicker ring edges may also be the physical manifestation of the ring's self-gravity plus pressure forces enforcing rigid precession across the ring (32).

Comparing the physical characteristics and structures observed in different regions across the rings can help in disentangling the various contributing effects that generate ring structure and in determining the magnitude of their contributions. Two contrasting regions within the inner B ring, seen at radial scales of ∼240 m/pixel, indicate the apparent sensitivity of ring-structure formation to the background optical depth. One region at 92,330 km (Fig. 5A) exhibits fine-scale irregular structure in a relatively high–optical depth (τ ∼ 1.5) part of the B ring, resembling in character the irregular structure seen in Voyager occultation and imaging data in equivalently high-τ parts of the B and A rings (33–35). However, irregular structure has never before been imaged at such a fine scale. Pulsation instability in dense rings may explain irregular structure on these length scales of 0.1 to 1 km (36). The second region in the B ring at 94,360 km (Fig. 5B), only ∼2000 km away, with τ ∼ 0.9, is puzzling in its lack of any fine-scale structure and instead supports smooth undulations in brightness of ∼100-km wavelength, with the bright bands in the image about 60 km across. These undulations are another form of unexplained structure and may be the result of a different physical mechanism. Ring regions of 100-km radial extent and reasonably high optical depth may exhibit sub-Keplerian shear rates because of the combined effects of finite particle size and physical adhesion between frost-covered particles. These regions would mimic an optically thick solid ring (34). Also, ballistic transport of material across ring regions resulting from meteoroid impacts (33) might also produce undulations of 100-km radial widths.

The outer portion of the B ring is among the densest in the rings (τ > 2), and the m = 2 radial distortion in its outer edge is maintained by the strongest resonance—the Mimas 2:1 ILR—in Saturn's rings (37). In Cassini SOI images, the region 300 km interior to the outer edge at 117,273 km (Fig. 5C) also exhibits irregular structure at a scale not seen before. Such structure, as well as the orientation and amplitude of the m = 2 distortion (the latter is a factor of 3.5 larger than that predicted by test particle resonant dynamics), may be the result of wave reflection and pulsation instabilities at the outer B-ring edge (38).

The Cassini division, the region between the A and B rings that is comparable to the C ring in color and optical depth (Fig. 2), was imaged during the SOI sequence. One of its broad, relatively featureless plateaus, with a mean optical depth τ ∼ 0.075 (39), sports a very weak linear density wave (40), resolved here for the first time, created by the Atlas 5:4 resonance (Fig. 5D). The most optically thick region of the Cassini division (Fig. 5E) shows a wave feature caused by the Prometheus 5:4 ILR—a dark 180-km wide band—and two diffuse bright bands, each about 65 to 70 km across, reminiscent of the inner B-ring structure (Fig. 5C) with optical depths ∼ 0.26. One of these bands also contains a weak Pan 7:6 ILR wave, which is not easily discernible in the image.

Analyses of the Pan and Atlas waves in the Cassini division have allowed determination of basic ring properties that had previously been determined with reasonable confidence only for the A and C rings. From a fit of the decrease of wavelength of the Atlas 5:4 wave with distance from resonance (fig. S4a), we infer a surface mass density σ = 1.4 ± 0.1 g/cm^2. The quantity $R_{eff} \equiv \sigma/(\tau\rho)$, where ρ is the internal density of a ring particle, is a measure of the effec-
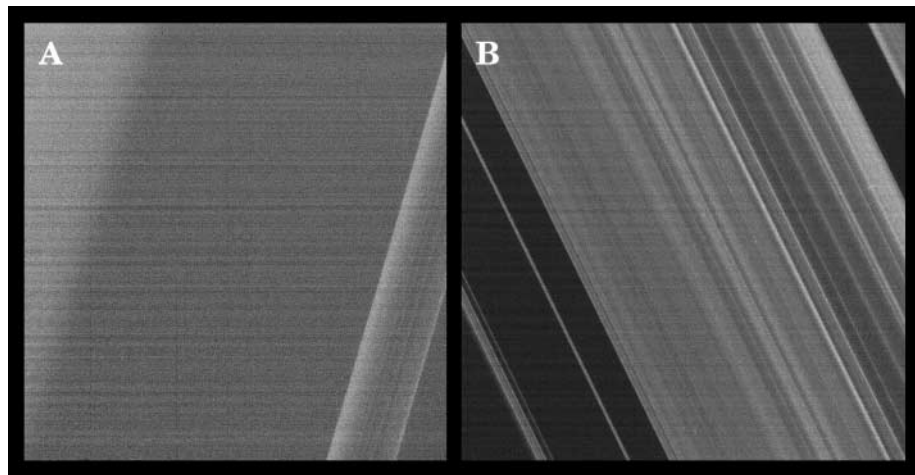
Fig. 4. Two SOI dark-side images of the Maxwell and Huygens ringlets, taken at a solar incidence angle of 114.5°. (**A**) The Maxwell ringlet is the band on the right, sitting in a gap of the same name. The image, N1467344214, is centered on 87,396 km, has a radial scale of 0.25 km/pixel, and was taken from a phase angle of 82° and an emission angle of 47°. A wave is faintly visible in the middle of it. A diffuse ringlet situated to the left of the Maxwell ringlet and discovered in later Cassini images (Fig. 7A) is not visible here. (**B**) The Huygens ringlet is the left-most narrow feature and appears alongside a very narrow ringlet and a broad plateau. This image, N1467345149, is centered at 118,009 km with a radial scale of 0.37 km/pixel and was taken from an emission angle of 63° and a phase angle of 59°. A diffuse narrow ringlet has also been found inward (to the left) of the Huygens ringlet (Fig. 7B), but is not visible here. Brightnesses measured across these ringlets have been converted to optical depth, τ, and compared with the Voyager PPS and RSS scans (2) (fig. S3).

tive size of the ring particles. Assuming $\rho = 0.6$ g/cm³, we find $R_{eff} \sim 30$ cm at the location of the Atlas 5:4 wave, comparable to the value measured in the optically thin inner C ring (41) but nearly an order of magnitude smaller than we and others have found in Saturn's A ring (42). Thus the effective particle size is ~ 10 times larger in the A ring (43, 44) than in the inner C ring and inner Cassini division. We also determined the viscosity, ν, for the Atlas 5:4 wave and found $\nu \sim 2$ cm²/s. Using the "classical" expression $\nu = c^2\tau/[2\Omega(1 + \tau^2)]$ (45), where c is the dispersion, or random, velocity of the ring particles and Ω is their orbital frequency, this implies $c \sim 0.1$ cm/s and a ring scale height $H = c/\Omega \sim 6$ m.

We derived the first estimate of the mass of Atlas from the amplitude of the 5:4 wave; the "nominal" gravitational mass of Atlas is $GM_{Atlas} = 0.00072$ km³/s² for an assumed density of 0.63 g/cm³ and a mean diameter of 32 km based on Voyager images (46). However, our best fit gives $GM_{Atlas} = 0.00014$ km³/s², i.e., a mass only $\sim 20\%$ of the nominal mass. As we discuss above, our modeling of unresolved Cassini images yields a diameter of 20 km for Atlas, implying a mean density for Atlas of 0.5 g/cm³. This density agrees well with the densities of 0.4 to 0.6 g/cm³ previously inferred for Epimetheus, Janus, Prometheus, and Pandora (13, 46–48).

We observed a large number of density waves due to Pan in the SOI image sequence. Resolved waves range from the 7:6 in the Cassini division to the 90:89 in the mid-A ring. For the 7:6 wave in the outer Cassini division, we obtained a surface density $\sigma = 2.5 \pm 0.3$ g/cm² from wave fits (fig. S4b). In this region, $\tau = 0.26$; again assuming $\rho = 0.6$ g/cm³ for the ring particles, we obtain $R_{eff} \sim 20$ cm, similar to the value we found in the inner Cassini division using the Atlas wave. The viscosity for the Pan 7:6 wave is 3.5 cm²/s, implying $H \sim 5$ m.

Because of the larger optical depth of this region, determining the mass of Pan is not as straightforward as it is for Atlas. Even though the Pan wave is linear, the relation between the observed I/F variations and the optical depth variations in the wave is nonlinear. Thus, the optical depth (or surface mass density) profile we infer is model dependent. Our best fit gave $GM_{Pan} = 0.00011$ km³/s², which corresponds to a density for Pan of only 0.19 g/cm³ if we take Pan's mean diameter to be the Cassini value of $D = 25.6$ km, or a density of 0.39 g/cm³ if we use Pan's pre-Cassini diameter of 20 km. Modeling of the Encke gap edge waves (see below), which is probably more reliable, gives a larger mass of $GM_{Pan} = (0.00033 \pm 0.00005)$ km³/s², leading to a density of 0.56 g/cm³ for $D = 25.6$ km or 1.18 g/cm³ for $D = 20$ km. Most likely, Pan has a density smaller than that of solid ice (0.92 g/cm²), like all the other satellites interior to Mimas with known densities.

The most optically thick region in the A ring (Fig. 5F), at a distance of 122,900 km and $\tau \sim 1.5$, shows irregular structure similar to that seen in other moderate– to high–optical depth regions in the rings but finer in scale. This is the finest structure seen anywhere in our images and may be evidence of the very long wave trains of undamped density waves, such as the Pandora 5:4 wave, which resides off the left-hand side of the image. A theoretical model of the damping of nonlinear density waves shows an abrupt transition in behavior with optical depth (49). Density waves in the moderate-τ outer A ring, such as the Mimas 5:3 wave, are predicted to have a wavelength (λ) that declines as x^{-1}, where x is the distance from resonance, as is observed, and also damp at roughly the predicted rate. Waves in slightly higher-τ regions, such as the inner B and A rings, are predicted to have $\lambda \sim x^{-1/3}$, contrary to observations, and to propagate essentially undamped forever. Although waves in high-τ regions, such as the Pandora 5:4, do propagate farther than waves in regions of smaller optical depth, all existing models underestimate damping of waves in high-τ regions (49–51).

The workings of strong satellite perturbations can be most clearly seen in SOI images of the A ring. A striking, uniformly spaced "corduroy" pattern overlain by two density waves is obvious in Cassini images (Fig. 5G) and provides the visual two-dimensional evidence for wakes excited by the satellite Pan (52, 53) embedded in the Encke gap (just off
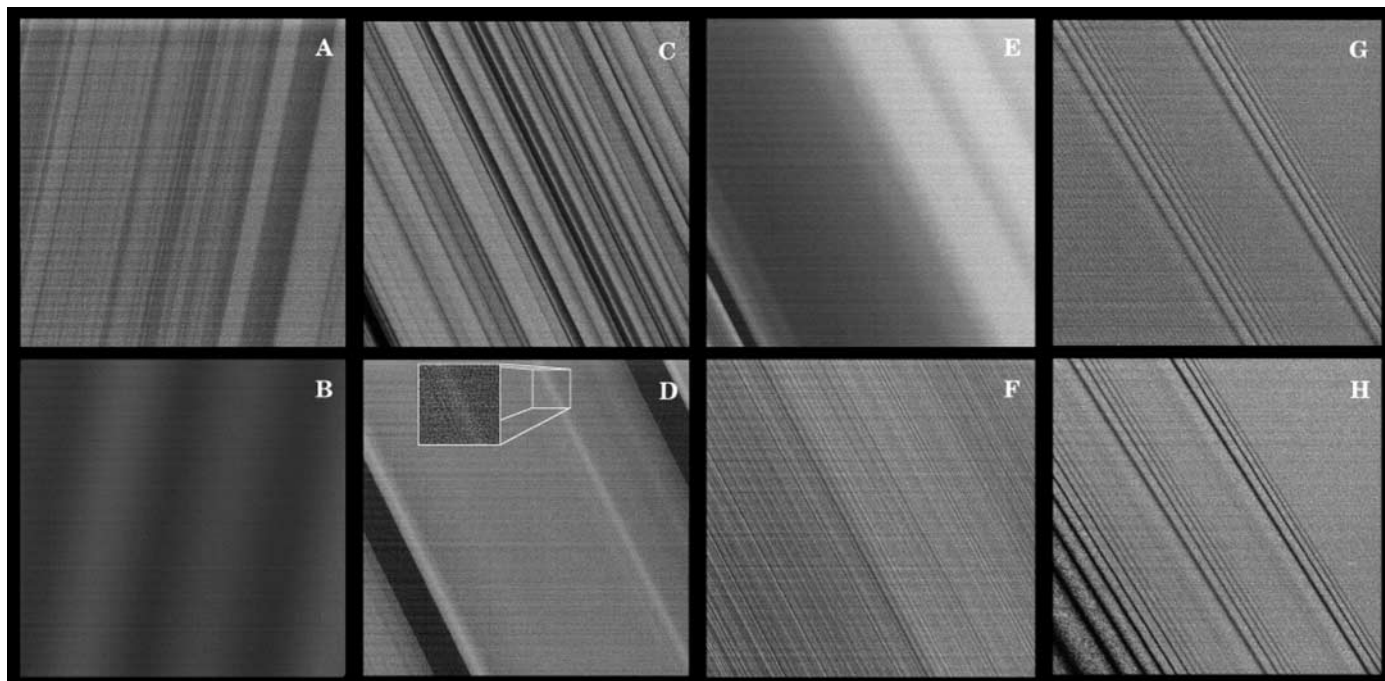

Fig. 5. This set of high-resolution images of Saturn's rings was taken during the dark-side SOI observation period with a solar incidence angle of 114.5°. Image scales range from 0.24 to 0.37 km/pixel in the ring plane. Images (**A**) and (**B**) were taken from an emission angle of 47° and a phase angle of 82°; images (**C**) through (**H**) were taken from an emission angle of 63° and a phase angle of 59°. Image names and radial locations of the centers of the images are as follows: (A) N1467344509, 92,326 km; (B) N1467344627, 94,362 km; (C) N1467345090, 117,273 km; (D) N1467345208, 118,745 km; (E) N1467345326, 120,496 km; (F) N1467345503, 122,893 km; (G) N1467346329, 133,227 km; and (H) N1467346447, 134,531 km.

the upper-right corner) less than ~200 km away. Wakes are created by the intersection of high–wave number, disturbed ring particle streamlines caused by the passage of Pan. The wakes in the "corduroy" pattern are produced in a manner identical to that of the waves seen on the inner edge of the Encke gap (see below), but here their wavelengths, amplitudes, and cant angles result from an encounter with Pan that was both more distant and further in the past. In fact, this region contains two wakes (fig. S5). The weaker, second-order wake was excited by Pan nearly two synodic periods earlier (1 synodic period = 0.39 years),

but persists superimposed upon the first-order wake. Pan wakes cross the entire region and interact with a pair of density waves excited by moons exterior to the rings. The persistence of the wakes far from Pan and the inferred lack of damping may signify the importance of collective effects and self-gravity in maintaining coherent structure far from the moon.

A collection of new ring phenomena was seen in the dark-side SOI sequence that may be evidence of different physical manifestations of particle aggregation, caused by either gravitational instabilities or kinematical

effects or both. The features known as "straw"—i.e., short-scale (a few kilometers), narrow, quasi-parallel variations in brightness—are seen in the first few troughs of strong density waves in dark-side SOI images of the rings. The most prominent examples are seen in the first troughs of the Janus 6:5 (Fig. 5H) and the Janus 4:3 density waves, as well as in the smaller Prometheus 33:32 wave ~55 km outside the Keeler gap. Other features, which show less prominent straw, are the Pandora 5:4, the Janus 2:1, the Pandora 9:8, the Mimas 5:3, and in the 3rd band/wake due to Pan ~13.5 km outside of the Encke gap. In most cases, straw is seen in several successive troughs of one wave, covering radial extents of dozens to greater than 100 km, fading out as the wave damps. One notable exception is the Prometheus 33:32 in which straw appears only in the first trough between the first two crests of the density wave. In all cases where straw is obvious, its longitudinal extent covers the entire field of view, which for dark-side images is less than 1°.

The most obvious examples of straw have length scales of a few kilometers. In Fig. 5H, the straw appearing in the broadest trough has a cant angle to the orbital motion of 11° in the trailing direction. "Light" straw has length scales typically on the order of 1 km or less, appearing most prominent closer to the wave peaks and less so in the very bottom of the trough.

Figure 6C is a dark-side SOI image of the outer edge of the Encke gap taken 18° upstream from Pan. Regularly spaced, ~6-km-wide bands bordered by the narrow dark lanes or wakes caused by Pan are visible. The ropy features seen between the first two wakes in Fig. 6C are unique in all Cassini images taken so far. They are generally between 10 and 20 km long and have a cant angle of 5° relative to the orbital direction in the trailing sense in the band closest to the gap, and ~9° in the next band out.

The straw and the ropy features appear similar to the transient, azimuthally limited, wakelike structures caused by gravitational instabilities in models originally used to explain the spiral arms of disk galaxies (54). Those structures are expected in the middle A ring and are believed to be responsible for the A-ring azimuthal brightness asymmetry. However, the observed scale in the rings is very different for the two phenomena: The gravitational wakes for the mid-A ring have length scales of ~120 m, whereas the straw is several kilometers long and the ropy structure at the outer edge of the Encke gap is tens of kilometers long. To explain the most prominent straw (in the Janus 6:5 wave) solely in terms of a gravitational instability would require a background surface mass density in the rings of $\sigma \sim 550$ g/cm². This is not reasonable given the optical depth of the
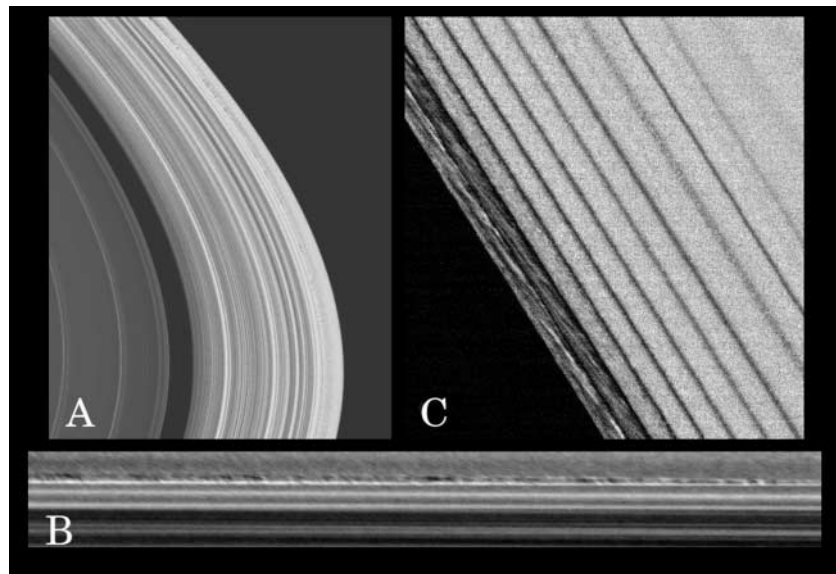

Fig. 6. Examples of two new ring phenomena: "mottled" and "ropy" structures. (**A**) Dayside SOI image of the outer edge of the A ring with solar incidence angle of 114.5°, an emission angle of 93.5°, and a phase angle of 129°. This image radial scale is 0.98 km/pixel. The longitudinal coverage is ~5.2°. (**B**) A map projection of the image (A), covering about 2.05° of longitude, roughly half of the full longitudinal extent seen in (A) and only 72 km in radial extent. (**C**) Dark-side SOI image N1467346388, with an incidence angle of 114.5°, an emission angle of 63°, and a phase angle of 59°, shows the outer edge of the Encke gap and the region exterior to it. The wakes of Pan are clearly seen. A different example of mottled structure is seen in the eighth Pan wake from the edge, as well as ropy structure within the first two bands exterior to the gap. This figure covers 180 km in radius and roughly 0.07° in longitude. The radial scale is 0.27 km/pixel and the longitudinal scale is 0.00013°/pixel.

Table 3. Measured radii and maximum brightnesses (*I/F*) for the diffuse ringlets seen in Fig. 7. "I" denotes inner; "O" denotes outer. The minimum optical depth needed to produce the *I/F* (assuming all forward-scattering dust), and the maximum optical depth needed to produce the *I/F* (assuming all large particles), are also given. These calculations assume that the observed *I/F* is due to single scattering. For R/2004 S1 and R/2004 S2, particular care was taken in subtracting out background scattered light (2). The main Encke ringlet at 133,581 km was detected in the Voyager PPS experiment, with a measured $\tau \sim 0.10$. (The semimajor axis of Pan is 133,584 km; the ring is coincident with the orbit of the moon.) If this optical depth applied to the Cassini ISS observation, the implied fractions, by optical depth, of dust and large particles are ~10% and 90%, respectively. However, this estimate is highly uncertain, because the main Encke ringlet is known to vary with longitude.

Diffuse ring	Radius (midpoint, km)	I/F	τ_{min}	τ_{max}
Maxwell I	87,418	2×10^{-4}	9×10^{-5}	0.05
Huygens I	117,744	5×10^{-4}	2×10^{-4}	0.04
Encke I	133,486	0.0048	0.003	0.04
Encke	133,581	0.0268	0.016	0.21
Encke O1	133,660	2×10^{-4}	1×10^{-4}	0.002
Encke O2	133,719	0.0019	0.001	0.015
Atlas (R/2004 S1)	137,630	6×10^{-5}	3×10^{-5}	3×10^{-4}
R/2004 S2	138,900	3×10^{-6}	1×10^{-5}	2×10^{-4}

region. Measured surface densities in the outer A ring are an order of magnitude smaller (42).

These features may be caused by a combination of gravitational and kinematical effects, as found in numerical simulations of the outer edge of the Encke gap (55). In that work, strawlike structures were produced, even in the absence of self-gravity, when particles were forced into close proximity as their streamlines were squeezed together in the wakes created by Pan; their cant angles changed with the changing phase of the material relative to the crest of the wave. However, when self-gravity was added, they were even more pronounced and become robust structures that look like the ropy features on the SOI dark-side image of the Encke gap. We surmise that the straw and ropy features are a product of enhanced kinematical and self-gravitational effects associated with passage of ring particles, and the consequent squeezing of their streamlines, through the crests of density waves or wakes.

An unusual mottled-looking narrow region, with a radial width varying with longitude from 5 to 10 km, was observed ~60 km inside the outer edge of the A ring (Fig. 6, A and B). This region is characterized by blotchy light and dark areas about 30 to 40 km in azimuthal extent. It does not cover the whole longitudinal extent of the images in which it appears (~5°), but radially narrows and fades to nothing near the ansa. The observed extent is ~3.5°, but the actual extent could be longer if it extends beyond the left-hand part of the image.

There are similar, narrow mottled-looking regions seen in the dark-side images, but none on such a large scale as that seen at the edge of the A ring. These others are observed in the dark crests of certain waves or in the wakes caused by Pan. The two most prominent of these are the eighth wake of Pan, about 69 km exterior to the Encke gap (Fig. 6C), and the first crest of the Pandora 13:12 (Fig. 5H). These both are about 3 km wide in the radial direction and extend over most of the field of view, ~1° in longitude.

The mottled regions are also probably caused by particle clumping that is longitudinally variable. The outer A ring is shaped into a seven-lobed pattern by a 7:6 Lindblad resonance with the co-orbital satellites, and the resonant perturbations in this region are complicated by the presence of many potential components with different pattern speeds, due to the presence of two satellites, Janus and Epimetheus, within 50 km of each other in orbital distance (37). It is possible that these perturbations, which extend 60 km inside the A ring, may be related to the co-orbital's non-axisymmetric perturbations in this region. The second type of mottling seen in the dark crests of waves and in the Pan wakes may be nothing more than extreme particle clumping that occurs in regions that are kinematically com-

pressed and eventually evolves into straw and ropy structure after the particles have passed through the crests/wakes and into the troughs.

We have discovered and measured the properties of new narrow tenuous rings between the A ring and the F ring and within some of the gaps in Saturn's main rings: i.e., Encke in the A ring, Huygens in the inner Cassini division, and Maxwell in the C ring (2) (Fig. 7 and Table 3). Ringlets had been observed inside the Encke gap in Voyager images, but the Cassini lit-side image shows the presence of three major ones and a rather tenuous one that may be nothing more than

an enhancement on a broader sheet of material. The center ringlet, which probably has the highest optical depth among the ringlets in Table 3, is coincident with Pan's orbit, implying that here, the ring particles are being maintained in horseshoe orbits (56–58). It, along with other ringlets in the Encke gap, exhibits longitudinal variations in brightness, suggestive of the particle accumulation that occurs in corotation sites associated with corotation resonances (58a).

It is not clear at present whether the origin of all these low–optical depth ringlets is the same. The association of the Atlas ring with Atlas and the main Encke ringlet with
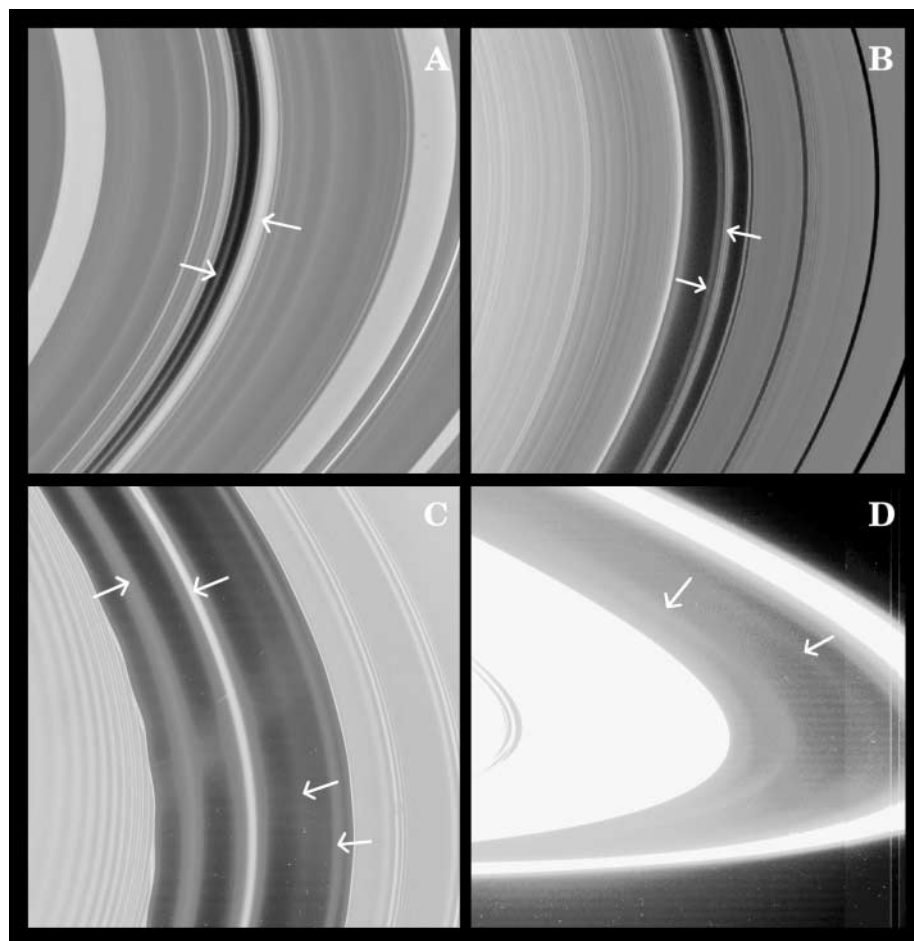

Fig. 7. Diffuse ringlets discovered within Saturn's rings. All images have been heavily processed to bring out low–optical thickness rings. Images (A) and (B) were taken with a solar incidence angle of 114.5°, an emission angle of 99°, and a phase angle of 145°. (A) Image N1477742794 is centered on a radius of 84,394 km, has a radial scale of 7 km/pixel, and shows a radial region of 4290-km extent, including the Maxwell gap in the C ring. The right arrow points to the optically thick Maxwell ringlet; the left arrow points to the new diffuse ring seen interior to it. (B) N1477740094 is centered on a radius of 117,292 km, has radial scale of 7 km/pixel, and covers 3870 km, including the Huygens gap immediately outside the outer B-ring edge. The right arrow points to the optically thick Huygens ring; the left arrow points to the new diffuse ring interior to it. Images (C) and (D) are from the dayside SOI sequence and have an incidence angle of 114.5° and an emission angle of ~94°. (C) Image N1467351325 is centered on a radius of 133,557 km interior to the Encke gap, has a radial scale of 1.15 km/pixel, a radial extent of 858 km, and was taken from a phase angle of 134°. The arrows point to (from the left) the Encke I, main Encke, Encke O1, and Encke O2 ringlets (Table 3). (D) This image is a composite of WAC images of the F-ring region taken from a phase angle of 87°. The radial scale is ~10 km/pixel. The left arrow points to R/2004 S1 (5) (the "Atlas" ring); the right arrow, to R/2004 S2 (4) (Table 3).

Pan would suggest that these rings derive from their associated moon. In other cases, a ring may exist because the material (or small parent bodies within it) are shepherded by a larger moon also present in the gap. The particles in many or all of the ringlets in Table 3 may have substantial fractions of micrometer-sized dust, implying that nongravitational forces may also affect the ringlets' dynamics. In any case, the presence of narrow diffuse ringlets in a gap like Maxwell and Huygens, along with the major Maxwell and Huygens ringlets, and the additional narrow ringlets in the Encke gap, suggests that there are other moonlets in these gaps.

Cassini images have shown clear evidence for two narrow strands of material on either side of the main core of the F ring: a 700-km-wide envelope of material surrounding the F ring, and an azimuthal structure within the ring and its envelope, some of which is clearly explained by interactions with Prometheus. Even though the F ring has been successfully modeled as an eccentric, inclined ring (59), its behavior in Cassini images suggests that it exhibits localized (and hence short-term) radial fluctuations, much of which is still unexplained.

A discontinuity in the ring and a streamer of material linking it with Prometheus (Fig. 8G) were observed in the vicinity of conjunction with Prometheus at its apoapse, reminiscent of the structures seen in the numerical modeling of a multistranded F ring perturbed by the moon (60, 61). These models provide qualitative explanations for such phenomena: The moon's perturbation switches sign at the encounter longitude, altering ring particle semimajor axes and eccentricities (60). Particles encountering Prometheus immediately before apoapse are dragged backward, whereas those encountering it just after apoapse are tugged forward. The induced changes in semimajor axis remove particles from the F-ring region, opening a gap (61); the affected particles form a stream of material approximately in the radial direction. Physical collisions with Prometheus are not the most important effect.

Some images showed evidence for streamers extending between the F-ring core and the outer and inner strands (Fig. 8, A and B, respectively). Others (Fig. 8, C and D) have shown that gradual radial displacement in the core extending over ~12° in longitude and peaking at ~60 km in radius appeared on one ansa and was detected as a mirror image reflected in the azimuthal direction, on the other ansa 8 hours later. This suggests that these structures are due to a gradual change in eccentricity along 12° of longitude followed by a sudden change of ~0.0002, giving rise to the kink. The symmetry arises because the particles at apoapse in the ansa in Fig. 8C will be at periapse in the ansa in Fig. 8D. A corollary of this is that a kink imaged at one longitude may appear as a clump at ± 90° from that longitude.
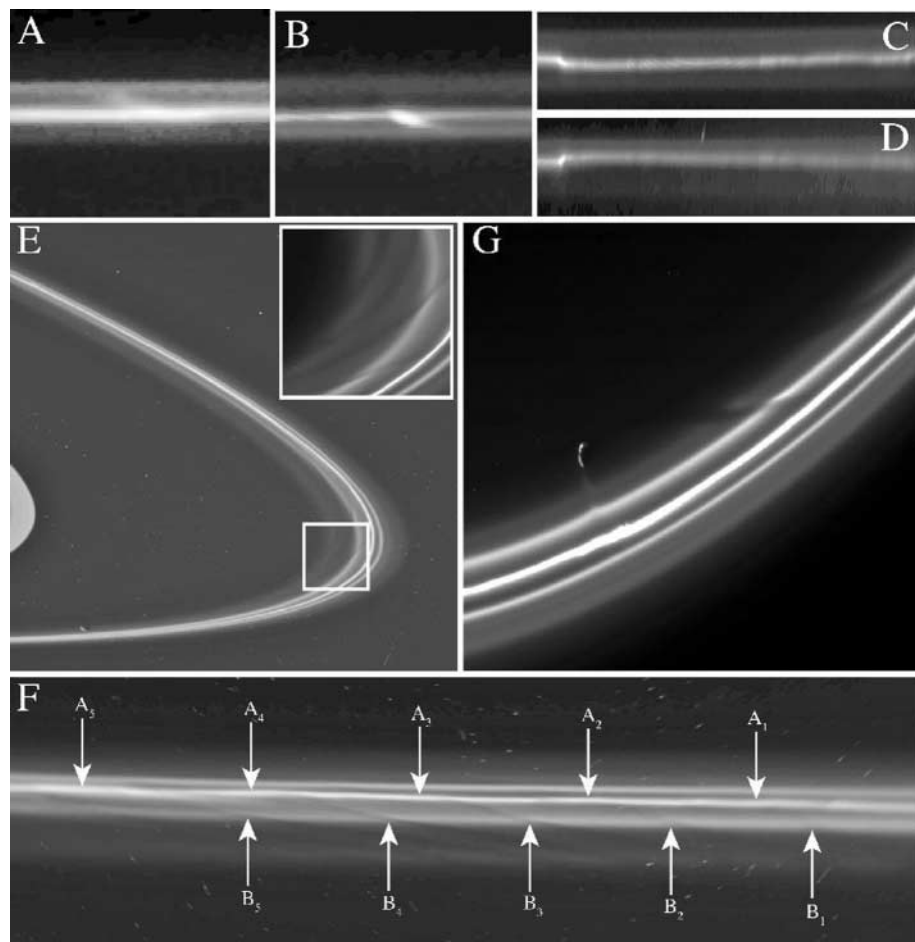

Fig. 8. (**A** and **B**) Evidence for material connecting the bright, central core of the F ring to the prominent outer and inner F-ring strands, respectively. Each reprojected image covers 6.25° of longitude and 2000 km in radius. (**C** and **D**) Images of a single reprojected section of 1000-km radial width of the F ring but separated by 8 hours and 193° in longitude. Evidence of reflective symmetry is apparent along ~12° in the azimuthal direction and in the mirrored "kink." (**E**) A view of the lit-face of the F-ring region taken on 1 July 2004 following the post-SOI descending ring plane crossing. The WAC image covers 7° in longitude at the edge of the A ring (seen on the left) and 27° at the F ring; Prometheus is visible at the lower left. The inset (top right) shows a simultaneously shuttered NAC image centered on the inner F ring. (**F**) A reprojection of the F ring region in (E) into a longitude-radius system centered on the ansa covering 18° in longitude and 1880 km in radius. The A- and B-labeled arrows denote the longitudes where Prometheus was at apoapse based on the relative mean motion of material in the core (59) and a strand with a semimajor axis that was 140 km interior to it, respectively. The observed slope in the reprojection is due to the eccentricity of the rings. (**G**) NAC image taken on 29 October 2004 showing the multiple strands of the F ring, a streamer of material connecting Prometheus with the F ring, and sheared gaps in the inner strands due to previous apoapse encounters with Prometheus.

Some of the clumps for which the F ring is renowned undoubtedly have their origin in this dynamic behavior caused by Prometheus.

At high resolution, two main strands are visible ~90 km exterior and ~140 km interior to the main F-ring core. Based on radial scans of the NAC, the estimated widths of the inner, core, and outer strands are 70, 20, and 30 km, respectively. All three of these rings are themselves embedded in the ~700-km-wide envelope seen in the enhanced image. Striations extending from the F-ring core, through the inner strand and into the interior dust sheet, take the appearance of "drapes" of material (Fig. 8E). The positions

of the gaps in between the drapes in the inner strand are clearly correlated with the positions of Prometheus when it reaches consecutive apoapses; the positions of azimuthal features in the core of the ring are not so well correlated with Prometheus's apoapses (Fig. 8F). Furthermore, the observed changing tilt of the drapes with longitude around the ring, and asymmetry in the tilt on either side of the gap, suggest that the striations are the result of the Keplerian shear of perturbed material that was approximately radial at the time of successive apoapse passages of Prometheus, consistent with the physical model for gap formation (60, 61) discussed above.

Fig. 9. Encke Gap. **(A)** Inner and **(B)** outer edges of the Encke gap as seen in Fig. 7C, mapped into a longitude-radius system, enhanced in contrast and brightness and radially stretched by a factor of 20.
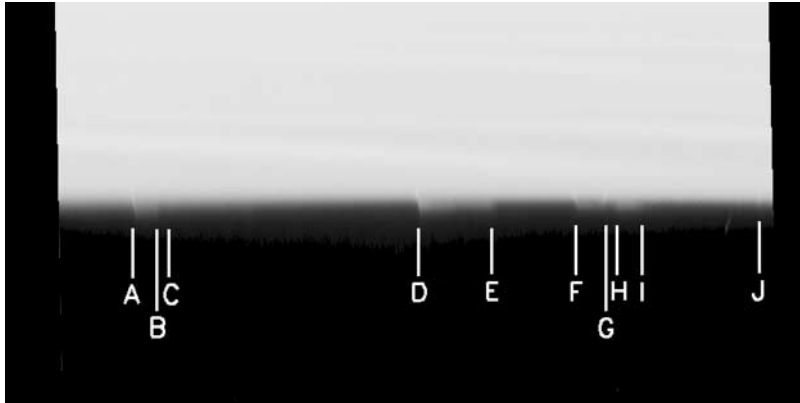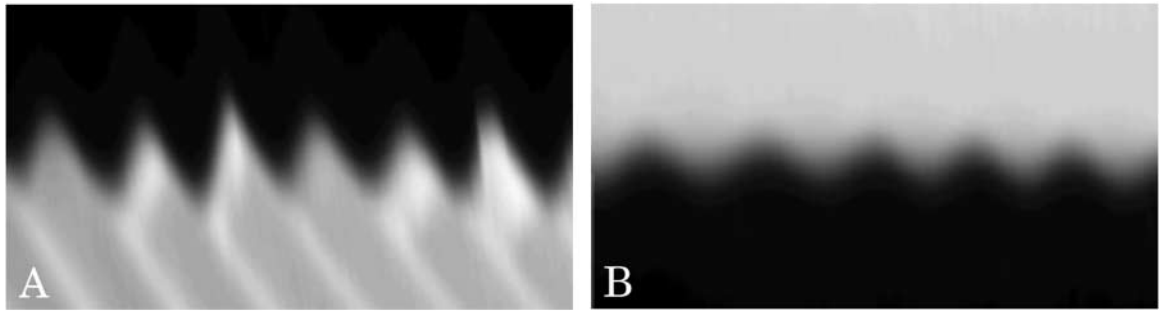

Fig. 10. Keeler gap. Spikes (sharp, radial discontinuities) and wisps (broad, faint material generally seen in between the spikes) observed in the outer edge of the Keeler gap during the SOI dayside sequence. The most easily seen features are labeled A through J. The image has been mapped into a longitude-radius system, contrast enhanced and radially stretched by a factor of 5. The longitudinal extent of the map is 4.6°; the radial extent, top to bottom, is ~60 km.

It is unlikely that Prometheus is the only perturber in the F ring. Small moons and short-lived "rubble piles" in the vicinity of the F ring have been proposed to explain a variety of Voyager (62–64) and ground-based (6, 65) observations. Fourier analyses of the azimuthal structures seen in the F-ring core in Cassini movie images covering an entire F-ring orbit have confirmed the periodic perturbations of Prometheus on the ring at a wavelength of 3.2°, and reasonably strong signatures between and including 5.0° and 6°. The latter may be the signature of Pandora, which should fall at 5.75°. However, they show no evidence of any signatures in the orbits of S/2004 S3, S/2004 S4, and S/2004 S6 (2), and with the exception of the signature of Prometheus, no signatures at the wavelengths found by previous investigators (63).

There is also a clear indication of material extending ~400 km beyond the edge of the A ring (Fig. 9), as well as two new diffuse rings: a ~300-km-wide ring of material, R/2004 S1, in the orbit of Atlas (5) and another ring, R/2004 S2 (4), comparable to the Atlas ring and immediately interior to Prometheus's periapse distance. These rings have I/F values comparable to those of the jovian ring (Table 3 and fig. S6). Prometheus's apoapse distance corresponds to the inner sharp boundary of the F ring's envelope. These observations indicate

that Prometheus has swept material from the region occupied by its orbit.

The SOI sequence captured dark- and lit-side views of the Encke gap and the unmistakable perturbations due to Pan—scallops on the inner edge and bright spiraling streamers radiating away from the same edge. When the image is mapped in longitude and radius, severely contrast enhanced, and stretched radially by a factor of 20, it is evident that the inner edge (Fig. 9A) sports a decidedly nonsinusoidal distortion; the outer edge (Fig. 9B), a more or less sinusoidal wave of lesser amplitude.

The simple theory for the impulse approximation, in which the wavelength of the perturbation produced by a satellite on a circular orbit is given by $3\pi x$, where x is the distance of the satellite from the ring particle, does not explain all the details seen in the edges of the Encke gap. The wavelengths and amplitudes of the undulations on the inner and outer edges have been measured by least-squares fitting of a sinusoidal wave form. Fourier analysis was also used to ascertain the presence of other wavelengths, especially in the nonsinusoidal inner edge. For the inner edge, the dominant wavelength by both methods is 0.67° and $ae \sim 1.6$ km, respectively. The semimajor axis of Pan, determined by this work (Table 1), is 133584.0 ± 1 km.

The locations of the gap's inner and outer edges are 133,423.5 ± 0.5 km and 133,745.1 ± 0.5 km (66, 67), respectively. The distance of Pan from the inner edge is then ~160 km. This is consistent with the distance computed from the wavelength of the observed wave on the inner edge—~165 km—given the uncertainties in the latter. The kinematical explanation for the wavelength of the inner-edge wave fits the observations.

Pan's longitude at the time of the image is 19.5°. The longitude of the center of the image is 32°. The particles comprising the inner-edge waves, consequently, are leading Pan by 12.5°, which amounts to ~19 wavelengths. Thus, the inner waves are probably not damped at all, and we can estimate Pan's mass from their amplitude. The standard treatment predicts $ae \sim 2.24 \ \mu a^3/x^2$, which gives $\mu = M_{Pan}/M_S \sim 8.7 \pm 1.3 \times 10^{-12}$, or $GM_{Pan} = 3.3 \pm 0.5 \times 10^{-4}$ km^3 s^{-2}. This is about three times larger than the value we derive for Pan's mass from the 7:6 linear density wave. The density wave analysis is likely to be in error for reasons previously given. However, neglect of either the self-gravity of the ring particles and/or the eccentricity of Pan in the kinematic edge wave analysis that forms the basis of the relation between wave amplitude and distance may also contribute to the discrepancy. The non-sinusoidal nature of the inner-edge wave hints that Pan's eccentricity is likely to be a factor.

Edge waves are seen in the outer Encke gap edge, in which the particles are trailing Pan by 348° or ~457 wavelengths: Their dominant wavelength is 0.81° and their amplitude $ae = 0.4$ km. The distance of Pan from the outer edge is ~161 km, a value that is not consistent with such a wavelength (which yields $x \sim 201$ km). Either Pan is not responsible for the waves seen in the outer edge (Fig. 9B) and they indicate the presence of another moonlet in the gap ~ 40 km interior to Pan, or the simple kinematic model for edge wave development by Pan does not apply to this edge. The second putative moonlet would have to be ~25% of Pan's mass, and for the same density, ~60% of Pan's size. Such a moon would have been easily detected in Cassini movie sequences of the Encke gap. On the other hand, it is hard to imagine a pro-

cess that would alter the wavelength/distance relation on the outer edge and not on the inner edge, because the ring material interior and exterior to Pan has comparable optical depths and therefore surface mass densities. Cassini images of the Encke gap, and the large number of wakes due to Pan and second- and third-order waves, suggest that there is far less damping than the simplest, streamline intersection treatment of this dynamical system would predict (*52*, *68*, *69*).

The Keeler gap, the narrow gap only ~250 km interior to the outer edge of the A ring, was also captured in the lit- and dark-side SOI image sequences. In Cassini images, the gap is ~42 km wide. Several faint discontinuities, or spikes, in the outer gap edge have been discovered in two NAC dayside images (Fig. 10); these are similar to the spikes protruding inward from the core of the F ring during Prometheus's passages (Fig. 8G). Wisps of faint material, vaguely reminiscent of the drapes and striations seen interior to the F ring, are seen in association with, and between, some of these spikes in the Keeler gap outer edge (Fig. 10). These features all move in unison at the Keplerian rate appropriate to the motion of particles at this location. Arguing on the basis of their similarity to the features caused by Prometheus in the F ring, it is likely that they are caused by the apoapse passages of a yet-unseen moonlet on an eccentric orbit within the Keeler gap. The spikes are ~5 km long. The putative moon would have a diameter of a few kilometers, scaling from the widths of the Encke and Keeler gaps and our inferred size for Pan (*28*). Interpreted in this way, measurement of their preferred length scale should indicate the position of the moonlet. To this end, correlations between the spikes' longitudinal positions and grids with a range of characteristic spacings were numerically calculated. The most statistically significant characteristic spacing was found to be 199 km at a 78% confidence level. A set of features with this particular wavelength, caused by a moon on an eccentric orbit, would be associated (through the $3\pi x$ relation) with a perturber at a radial separation of 21 km, which is half the width of the Keeler gap. These observations indicate that there is a tiny moon orbiting at the center of the Keeler gap.

Finding any feature in the outer part of the A ring that is certifiably circular is difficult; almost all features in this region are noncircular density waves or nonaxisymmetric edges. Taking the outer edge of the Keeler gap to be circular (despite the presence of the short spatial scale spikes and wisps), streamerlike features exterior to the outer Keeler gap edge are then spiral in nature, like those seen spreading away from the inside of the Encke gap edge. These may be wake structures caused by the putative Keeler moon.

References and Notes

1. C. C. Porco *et al.*, *Space Sci. Rev.* **115**, 363 (2004).
2. See supporting data in *Science* Online.
3. C. C. Porco *et al.*, *IAU Circ.* **8389**, 1 (2004).
4. C. C. Porco *et al.*, *IAU Circ.* **8432**, 1 (2004).
5. C. C. Porco *et al.*, *IAU Circ.* **8401**, 1 (2004).
6. J. M. Barbara, L. W. Esposito, *Icarus* **160**, 161 (2002).
7. P. Thomas, J. Veverka, D. Morrison, M. Davies, T. V. Johnson, *J. Geophys. Res.* **88**, 8743 (1983).
8. N. Borderies, P. Goldreich, S. Tremaine, in *Planetary Rings*, R. Greenberg, A. Brahic, Eds. (Univ. of Arizona Press, Tucson, AZ, 1984), pp. 713–734.
9. J. Scargle *et al.*, *Bull. Am. Astron. Soc.* **25**, 1103 (1993).
10. J. A. Burns, B. J. Gladman, *Planet. Space Sci.* **46**, 1401 (1998).
11. R. A. Jacobson, *Bull. Am. Astron. Soc.* **36**, 1097 (2004).
12. P. Goldreich, R. Sari, *Astrophys. J.* **585**, 1024 (2003).
13. R. A. Jacobson, R. G. French, *Icarus* **172**, 382 (2004).
14. J. N. Cuzzi, R. G. French, L. Dones, *Icarus* **158**, 199 (2002).
15. The reflectivity of a surface is given in terms of *I/F*, where *I* is the intensity of the scattered light and πF is the net flux of solar radiation per unit area normal to itself (*70*). Spectral slope is defined as $d(I/F)/d\lambda \div (I/F)_0$, where $(I/F)_0$ is the value of *I/F* at some fiducial wavelength. Ground-based observations have shown that the main rings are "red" in the spectral range from 300 to ~600 nm (i.e., *I/F* increases with wavelength, λ), whereas *I/F* is roughly constant from 600 to 1000 nm (*71*, *72*). HST observations showed that the rings' spectral slope increases with phase angle over the range 0° to 6° visible from Earth. This reddening is thought to result from multiple scattering within the surfaces of ring particles (*14*). Our results show that little, if any, additional "phase reddening" occurs at phase angles between 6° and 66°. Color variations in Saturn's rings on a variety of spatial scales have been seen by Voyager and HST (*16*, *73*, *74*).
16. J. N. Cuzzi *et al.*, in *Planetary Rings*, R. Greenberg, A. Brahic, Eds. (Univ. of Arizona Press, Tucson, AZ, 1984), pp. 73–199.
17. F. Poulet, J. N. Cuzzi, *Icarus* **160**, 350 (2002).
18. F. Poulet, D. Cruikshank, J. N. Cuzzi, T. L. Roush, R. G. French, *Astron. Astrophys.* **412**, 305 (2003).
19. L. R. Doyle, L. Dones, J. N. Cuzzi, *Icarus* **80**, 104 (1989).
20. J. N. Cuzzi, P. R. Estrada, *Icarus* **132**, 1 (1998).
21. B. A. Smith *et al.*, *Science* **212**, 163 (1981).
22. C. A. McGhee *et al.*, *Icarus*, in press.
23. T. Nitter, O. Havnes, F. Melandsø, *J. Geophys. Res.* **103**, 6605 (1998).
24. The interpretation of dark-side images can be ambiguous: Empty space, as well as high–optical depth regions, can appear; intermediate–optical depth regions appear bright.
25. C. C. Porco *et al.*, *Icarus* **60**, 1 (1984).
26. C. C. Porco, *Adv. Space Res.* **10**, 221 (1990).
27. Density waves are often referred to by the notation $(m + n + p):(m - 1)$, where *m*, *n*, and *p* are integers. This ratio is approximately equal to the ratio of the mean motions of the ring particle and the satellite that produces the wave. For a linear wave, the amplitude is proportional to $M_s e^p (\sin i)^n$, where M_s, *e*, and *i* are the mass, orbital eccentricity, and inclination to Saturn's equator of the satellite, respectively. For a given moon, the strongest density waves have $p = n = 0$, so that these waves are of the form $m:(m - 1)$. Waves driven by interior moons on exterior rings, like the Uranian ε ring, would have $(m - 1)$:m for first-order waves, and $(m - 2)$:m for second-order waves. The waves we describe in detail are Atlas and Pan waves with $m = 5$ and 7, respectively.
28. P. Goldreich, C. C. Porco, *Astron. J.* **93**, 730 (1987).
29. J. C. B. Papaloizou, D. N. C. Lin, *Astrophys. J.* **331**, 838 (1988).
30. C. C. Porco, thesis, California Institute of Technology (1983).
31. E. Turtle, C. C. Porco, V. Haemmerle, W. Hubbard, R. Clark, *Bull. Am. Astron. Soc.* **23**, 1179 (1991).
32. E. I. Chiang, P. Goldreich, *Astrophys. J.* **540**, 1084 (2000).
33. L. J. Horn, J. N. Cuzzi, *Icarus* **119**, 285 (1996).
34. S. Tremaine, *Astron. J.* **125**, 894 (2003).
35. E. Griv, M. Gedalin, *Planet. Space Sci.* **51**, 899 (2003).
36. J. Schmidt, H. Salo, *Phys. Rev. Lett.* **90**, 061102 (2003).
37. C. Porco, G. E. Danielson, P. Goldreich, J. B. Holberg, A. L. Lane, *Icarus* **60**, 17 (1984).
38. F. Namouni, C. Porco, *Bull. Am. Astron. Soc.* **34**, 884 (2002).
39. L. W. Esposito, M. O'Callaghan, R. A. West, *Icarus* **56**, 439 (1983).
40. F. H. Shu, in *Planetary Rings*, R. Greenberg, A. Brahic, Eds. (Univ. of Arizona Press, Tucson, AZ, 1984), pp. 513–561.
41. P. A. Rosen, J. J. Lissauer, *Science* **241**, 690 (1988).
42. L. J. Spilker *et al.*, *Icarus* **171**, 372 (2004).
43. H. A. Zebker, E. A. Marouf, G. L. Tyler, *Icarus* **64**, 531 (1985).
44. R. G. French, P. D. Nicholson, *Icarus* **145**, 502 (2000).
45. P. Goldreich, S. D. Tremaine, *Icarus* **34**, 227 (1978).
46. P. D. Nicholson, D. P. Hamilton, K. Matthews, C. F. Yoder, *Icarus* **100**, 464 (1992).
47. C. A. McGhee, P. D. Nicholson, R. G. French, K. J. Hall, *Icarus* **152**, 282 (2001).
48. S. Renner, B. Sicardy, R. G. French, *Icarus*, in press.
49. F. H. Shu, L. Dones, J. J. Lissauer, C. Yuan, J. N. Cuzzi, *Astrophys. J.* **299**, 542 (1985).
50. N. Borderies, P. Goldreich, S. Tremaine, *Icarus* **63**, 406 (1985).
51. N. Borderies, P. Goldreich, S. Tremaine, *Icarus* **68**, 522 (1986).
52. M. R. Showalter, J. N. Cuzzi, E. A. Marouf, L. W. Esposito, *Icarus* **66**, 297 (1986).
53. L. J. Horn, M. R. Showalter, C. T. Russell, *Icarus* **124**, 663 (1996).
54. W. H. Julian, A. Toomre, *Astrophys. J.* **146**, 810 (1966).
55. M. C. Lewis, G. R. Stewart, *Icarus*, in press.
56. S. F. Dermott, T. Gold, A. T. Sinclair, *Astron. J.* **84**, 1225 (1979).
57. S. F. Dermott, C. D. Murray, A. T. Sinclair, *Nature* **284**, 309 (1980).
58. S. F. Dermott, C. D. Murray, *Icarus* **48**, 1 (1980).
58a. C. C. Porco, *Science* **253**, 995 (1991).
59. A. S. Bosh, C. B. Olkin, R. G. French, P. D. Nicholson, *Icarus* **157**, 57 (2002).
60. M. R. Showalter, J. A. Burns, *Icarus* **52**, 526 (1982).
61. S. M. Giuliatti Winter, C. D. Murray, M. K. Gordon, *Planet. Space Sci.* **48**, 817 (2000).
62. J. N. Cuzzi, J. A. Burns, *Icarus* **74**, 284 (1988).
63. R. A. Kolvoord, J. A. Burns, M. R. Showalter, *Nature* **345**, 695 (1990).
64. C. D. Murray, M. K. Gordon, S. M. Giuliatti Winter, *Icarus* **129**, 304 (1997).
65. F. Poulet, B. Sicardy, P. D. Nicholson, E. Karkoschka, J. Caldwell, *Icarus* **144**, 135 (2000).
66. P. D. Nicholson, M. L. Cooke, E. Pelton, *Astron. J.* **100**, 1339 (1990).
67. R. G. French *et al.*, *Icarus* **103**, 163 (1993).
68. J. N. Cuzzi, J. D. Scargle, *Astrophys. J.* **292**, 276 (1985).
69. N. Borderies, P. Goldreich, S. Tremaine, *Icarus* **80**, 344 (1989).
70. S. Chandrasekhar, *Astrophys. J.* **106**, 152 (1947).
71. K. Lumme, H. J. Reitsema, *Icarus* **33**, 288 (1978).
72. E. Karkoschka, *Icarus* **111**, 174 (1994).
73. P. R. Estrada, J. N. Cuzzi, *Icarus* **122**, 251 (1996).
74. P. R. Estrada, J. N. Cuzzi, M. R. Showalter, *Icarus* **166**, 212 (2003).
75. G. W. Null, E. L. Lau, E. D. Biller, J. D. Anderson, *Astron. J.* **86**, 456 (1981).
76. We acknowledge the many individuals across the imaging team who have assisted in the design of imaging sequences and camera commands and in other vital operational and image-processing tasks, in particular E. Birath, J. Riley, B. Knowles, C. Clark, M. Belanger, and D. Wilson. M. Hedman is acknowledged for fruitful discussions. This work has been funded by NASA/JPL, the UK Particle Physics and Astronomy Research Council, the German Aerospace Center (DLR), and Université Paris VII Denis Diderot, Commissariat à l'Energie Atomique, Astrophysique Interactions Multiéchelles, France.